引用格式：WAN Zehong, DENG Hongyang, LEI Yu, et al. Low-damage Micromachining for 4H-SiC Pressure Sensitive Diaphragm by Femtosecond Laser[J]. Acta Photonica Sinica, 2023, 52(1):0114004
万泽洪,邓鸿洋,雷宇,等.4H-SiC压力敏感膜片的低损伤飞秒激光加工[J].光子学报,2023,52(1):0114004

4H-SiC压力敏感膜片的低损伤飞秒激光加工

万泽洪[1],邓鸿洋[1],雷宇[2],陶国裔[1],胡红坡[3],周圣军[1,2]
(1 武汉大学 工业科学研究院,武汉 430072)
(2 武汉大学 动力与机械学院,武汉 430072)
(3 广东科学技术职业学院 汽车工程学院,珠海 519090)

摘 要:采用飞秒激光加工4H-SiC压力敏感膜片,研究了飞秒激光深度方向步进间距、扫描路径方向、单脉冲能量、扫描线间距等参数对4H-SiC烧蚀形貌和烧蚀速率的影响。实验结果表明,飞秒激光加工4H-SiC样品表面孔洞的形成主要与激光诱导微沟槽的重叠有关,激光能量分布更均匀能够有效减少4H-SiC被烧蚀表面的激光诱导微沟槽的数量,增大激光扫描路径与激光偏振方向的夹角能够有效降低激光诱导微沟槽的重叠概率,从而抑制孔洞的形成。采用优化后的飞秒激光加工工艺参数,制备出直径为1 600 μm、厚度为100 μm的4H-SiC压力敏感膜片。所制备的4H-SiC压力敏感膜片表面无明显孔洞,边缘过烧蚀深度小于10 μm,实现了4H-SiC压力敏感膜片的低损伤飞秒激光加工。

关键词:微纳加工;压力敏感膜片;飞秒激光烧蚀;碳化硅;表面形貌
中图分类号:TN249 **文献标识码**:A **doi**:10.3788/gzxb20235201.0114004

0 引言

随着人们对极端环境探索的深入,发展用于恶劣环境的压力传感器变得更加重要。传统硅基压力传感器在200 ℃以上环境中工作时,p-n结反向漏电流增大导致传感器的电学性能受到影响[1-4]。当温度升高至400 ℃时,Si材料的机械性能大大退化,极大地影响了传感器的测量精度、工作量程和寿命[4-7]。碳化硅(SiC)是第三代半导体的代表材料,具有宽禁带(~3.2 eV)、高热导率、高击穿电场强度等物理性能以及优良的机械性能和化学稳定性,是制作恶劣环境下工作器件和大功率电子器件的理想材料,具有很好的应用前景[8-10]。

制作SiC压力敏感元件时,需要在SiC衬底表面加工盲孔以获得敏感膜片。SiC是一种脆性材料,具有很高的硬度(莫氏硬度为9.0~9.5),难以采用传统的机械加工工艺[11-12]。此外,Si-C原子间的强化学键使得室温下湿法腐蚀工艺不再适用[3,13]。目前常采用熔盐腐蚀、等离子体刻蚀、激光烧蚀等工艺加工SiC材料[13-23]。熔盐腐蚀是指采用熔融状态碱,如熔融氢氧化钾(KOH)等,腐蚀SiC材料。由于熔融KOH腐蚀SiC具有各向异性[14-16],且位错区域优先被腐蚀,因此熔盐腐蚀通常用于揭示SiC外延层的位错情况。等离子体刻蚀是目前最广泛研究和应用的SiC加工方式,包括反应离子刻蚀、深反应离子刻蚀、电感应耦合等离子体(Inductively Coupled Plasma, ICP)刻蚀、磁中性环路放电等离子体刻蚀等[17-20]。等离子体刻蚀需要先在SiC材料表面图形化一定厚度的刻蚀掩膜(如光刻胶、二氧化硅或金属等),然后采用氟基或氯基等离子体与SiC材料反应生成挥发性产物,实现SiC材料的选择性去除[17-18]。等离子体对SiC的刻蚀速率通常小于1 μm/min,降低了传感器的加工效率[17,19]。刻蚀掩膜图形化的过程使得SiC材料的加工变得复杂,降低了加工良率。随着SiC目标刻蚀深度的增加,掩膜的厚度需要增加,掩膜的制造难度也随之增加。因此,SiC的

基金项目:国家自然科学基金(Nos.52075394, 51675386, 51775387),国家重点研发计划(No. 2017YFB1104900),国家万人计划青年拔尖人才支持计划资助项目
第一作者:万泽洪,wanzh17@whu.edu.cn
通讯作者:胡红坡,huhongpo@tsinghua.org.cn;周圣军,zhousj@whu.edu.cn
收稿日期:2022-06-12;**录用日期**:2022-09-08

深腔刻蚀需要一种更为高效的加工方式来取代等离子体刻蚀。

激光烧蚀是一种高效加工SiC材料的方式。根据激光的单脉冲时间长短，可将工作激光分为纳秒激光、皮秒激光和飞秒激光[9, 21-23]。相比于纳秒激光和皮秒激光，飞秒激光与材料作用时间极短，且峰值功率高，多光子电离及碰撞电离成为它去除材料的主要方式[22]。飞秒激光加工具有热效应小、对材料损伤小、加工速率快、不需要掩膜、对晶体取向不敏感、能够形成复杂结构等特点，被国内外学者广泛研究[23-32]。ZHAO You等[32]采用1 064 nm飞秒激光加工了直径为1 200 μm、深度为270 μm的4H-SiC盲孔，得到了80 μm厚的压力敏感膜片。但敏感膜片呈椭圆形，且在敏感膜片边缘存在过烧蚀现象，过烧蚀沟槽的宽度和深度分别为56.2 μm和68.6 μm，需要进一步优化工艺。WANG Lukang等[23]采用1 028 nm飞秒激光加工了直径为1 200 μm、深度为270 μm的4H-SiC盲孔，并结合ICP刻蚀工艺降低了烧蚀表面的缺陷和表面粗糙度，得到了80 μm厚的敏感膜片。该方法需要使ICP的刻蚀速率与飞秒激光的烧蚀深度相匹配，才能实现4H-SiC敏感膜片厚度的精确控制。此外，在4H-SiC被烧蚀表面出现了孔洞，且孔洞无法通过ICP刻蚀完全消除。因此，需要进一步探究孔洞形成的原因，避免孔洞的形成。

为了探究飞秒激光加工4H-SiC材料的特性，本文研究了飞秒激光深度方向步进间距、扫描方向、单脉冲能量、扫描线间距等参数对4H-SiC材料表面形貌和烧蚀速率的影响。优化后的4H-SiC压力敏感膜片的加工工艺，制备出直径为1 600 μm、深度为250 μm、厚度为100 μm的4H-SiC盲孔，表面无明显孔洞。

1 实验

采用北京天科合达半导体股份有限公司生产的测试级N型掺杂4H-SiC衬底进行实验，其参数如表1所示。在飞秒激光加工压力敏感膜片之前先将4H-SiC晶圆切割成2 cm×2 cm的小片。图1为实验装置的原理图。采用190 fs掺镱钨酸钆钾晶体飞秒激光(Yb:KGW-based，Pharos，Light Conversion，1 028 nm)微纳加工系统烧蚀4H-SiC衬底的c面，加工系统的技术指标如表2所示。系统采用5倍显微镜，数值孔径NA=0.14 mm。飞秒激光的偏振方向垂直于X轴。在焦平面上，激光光斑直径为26 μm。所有实验均在20 ℃空气环境中进行，激光参数和平台移动路径均由电脑控制。

表1 4H-SiC衬底规格

Table 1 Specifications of the 4H-SiC wafer

Parameters	Valves
Diameter	99.5～100 mm
Thickness	350 μm
Surface roughness	≤1 nm
Conduction type	N-type
Doping type	Nitrogen
Doping concentration	$1\sim2\times10^{19}$ cm^{-3}
Wafer orientation	Off axis: 4° toward <11-20>±0.5°
Resistivity	0.015～0.028 Ω·cm

图2为飞秒激光加工4H-SiC压力敏感膜片的示意图，其中θ为激光扫描路径与激光偏振方向的夹角，Δd为扫描线间距，ΔH为深度方向的步进间距。图2(b)和(c)显示了平行线扫描和同心圆扫描两种不同的加工路径，图2(d)和(e)显示了圆柱形和圆台形两种材料去除方式。实验中，将样品安装在Aerotech XYZ三轴定位系统上，平台移动精度<0.25 μm。激光焦平面固定不变，随着3轴定位平台的移动逐层去除4H-SiC，直到平台移动高度达到设定值。加工完成后，依次采用无水乙醇、浓度为20%的HF(氢氟酸)超声清洗5 min，然后采用去离子水冲洗干净，N_2吹干。采用Zygo Newview 9000型光学轮廓仪测量4H-SiC的烧蚀深度H和被加工表面均方根(Root Mean Square，RMS)粗糙度S_q。采用TESCAN MIRA 3型场发射扫描电子显微镜(Scanning Electron Microscope，SEM)对被加工表面形貌进行表征。

飞秒激光光束为高斯光束，光束横截面的电场振幅和光强分布为高斯函数[33]，如图3所示。w_0为光束束腰半径；z为离束腰的距离；$w(z)$为电场振幅为轴上幅值的1/e时的半径，称为光斑尺寸；r为光束横截面

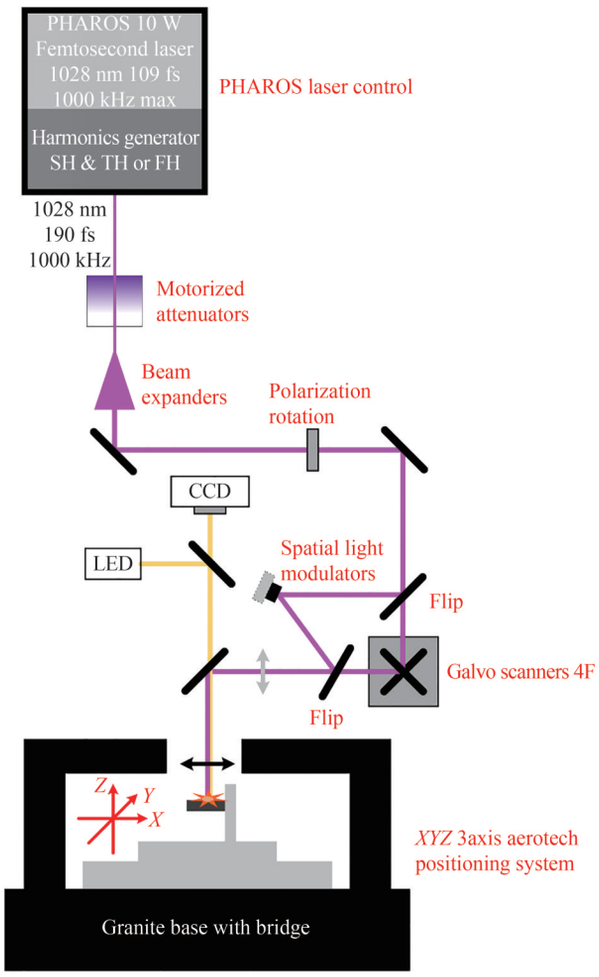

图1　飞秒激光实验装置示意图

Fig.1　Schematic illustration of the femtosecond laser micromachining system

表2　飞秒激光微加工系统参数

Table 2　Technical parameters of the femtosecond laser micromachining system

Parameters	Valves
Centre wavelength	1 028 nm
Pulse duration	190 fs
Frequency	200 kHz
Maximum power	10 W
NA	0.14 mm
Beam quality	$M^2 \leqslant 1.24$
Dot density	2 000/mm
Number of pulses per dot	1

内离光轴的距离。在光束横截面内，高斯光束的电场振幅$E(r)$和光强$I(r)$分别为

$$\begin{cases} E(r)=E_0(z)\mathrm{e}^{-\frac{r^2}{w(z)^2}} \\ I(r)=I_0(z)\mathrm{e}^{-\frac{2r^2}{w(z)^2}} \end{cases} \tag{1}$$

式中，$E_0(z)$、$I_0(z)$分别为$r=0$处的电场振幅和光强。飞秒激光传输时，每个横截面的强度分布仍然是高斯函数，但是沿着光轴方向强度轮廓的宽度产生变化。在束腰位置宽度最小，直径为$2w_0$，光斑尺寸沿着光轴变化的规律为

$$\begin{cases} w(z)=w_0\sqrt{1+\left(\dfrac{z}{z_R}\right)^2} \\ z_R=\dfrac{\pi {w_0}^2}{\lambda} \end{cases} \tag{2}$$

式中，z_R为瑞利长度；λ为激光波长。在瑞利长度处，光斑面积为束腰面积的2倍，即$w(z_R)=\sqrt{2}\,w_0$。

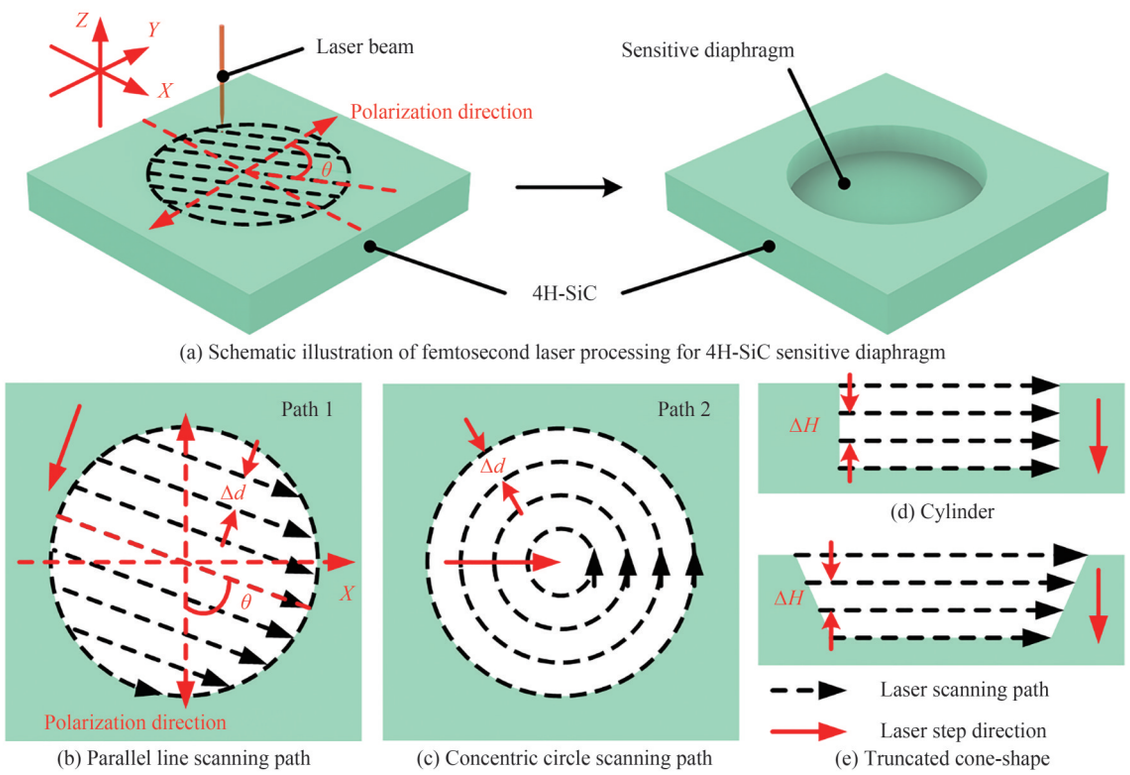

图2 飞秒激光加工4H-SiC敏感膜片示意图

Fig.2 Schematic illustration of femtosecond laser processing for 4H-SiC sensitive diaphragm

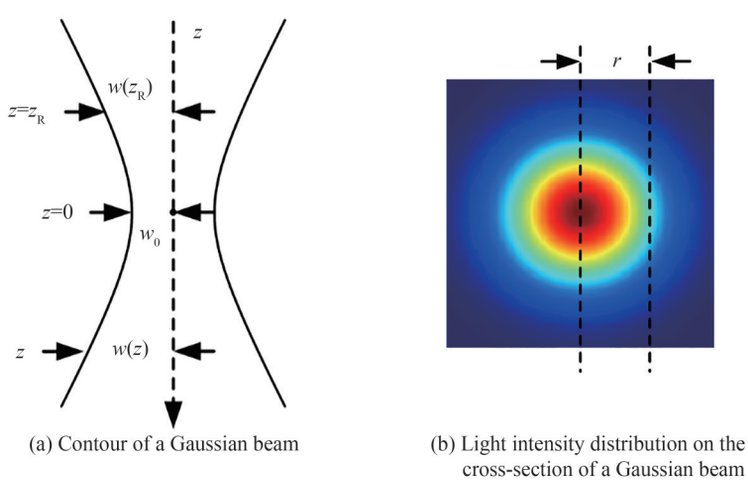

图3 高斯光束轮廓和光强分布示意图

Fig.3 Schematic illustration of the profile and light intensity distribution of a Gaussian beam

在半径t范围内的桶中功率为$P(t)$为

$$P(t)=\int_0^t 2\pi r I(r)\,\mathrm{d}r=\frac{\pi}{2}w(z)^2 I_0(z)\left(1-\exp\left(-2\frac{t^2}{w(z)^2}\right)\right) \tag{3}$$

则总功率P_t为

$$P_t=\lim_{r\to\infty}\frac{\pi}{2}w(z)^2I_0(z)\left(1-\exp\left(-2\frac{r^2}{w(z)^2}\right)\right)=\frac{\pi}{2}w(z)^2I_0(z) \tag{4}$$

根据能量守恒，不同横截面内的桶中功率相等，即

$$P_t=\frac{\pi}{2}w_0{}^2I_0 \tag{5}$$

因此，高斯光束总功率为束腰处最大光强与面积的乘积的一半。由式(4)可知

$$I_0(z)=\frac{2P_t}{\pi w(z)^2} \tag{6}$$

因此，飞秒激光传播路径上光强的一般分布为

$$I(z,r)=\frac{2P_t}{\pi w(z)^2}\exp\left(-\frac{2r^2}{w(z)^2}\right)=\frac{2P_t}{\pi w_0{}^2\left(1+\left(\frac{z}{z_R}\right)^2\right)}\exp\left(-\frac{2r^2}{w_0^2\left(1+\left(\frac{z}{z_R}\right)^2\right)}\right) \tag{7}$$

图4显示了飞秒激光传播路径的不同横截面上的光强分布和桶中功率分布，其中以$w(z)=100\times w_0$处的z值为脱焦位置。从图中可以看出，随着横截面逐渐远离束腰位置，激光光斑能量逐渐发散，桶中功率的增长速度逐渐变慢。在$z=z_R$的横截面内，其峰值光强为束腰位置峰值光强的一半。

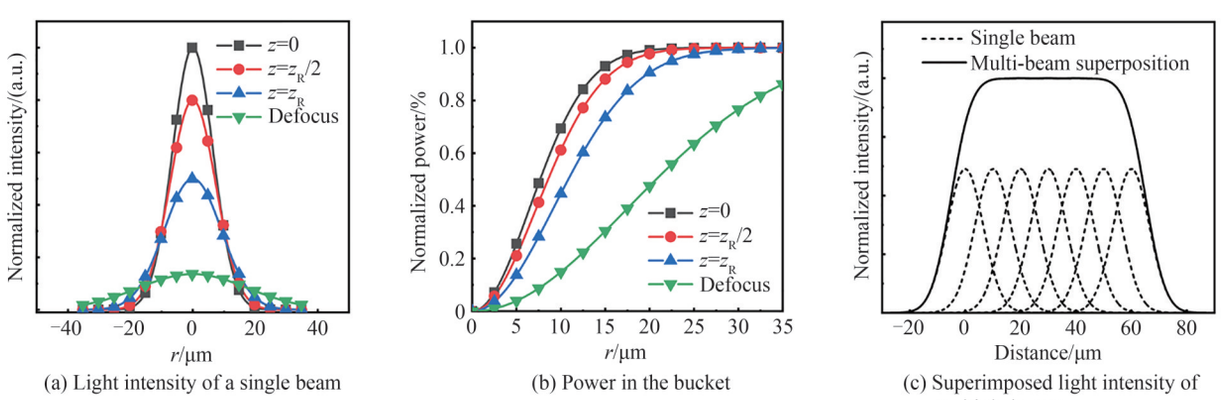

(a) Light intensity of a single beam　(b) Power in the bucket　(c) Superimposed light intensity of multiple beams

图4　飞秒激光的能量分布

Fig.4　Energy distribution of the femtosecond laser

由于扫描线间距Δd小于光斑直径，因此同一横截面内扫描路径之间存在部分重叠，产生不同时间上光斑能量的重合。4H-SiC被加工表面在同一横截面内的叠加光强分布表达式为式(8)，其分布如图4(c)所示。

$$\sum_{i=0}^{n}I(z,r+\Delta d\cdot i)=\sum_{i=0}^{n}\frac{2P_t}{\pi w_0{}^2\left(1+\left(\frac{z}{z_R}\right)^2\right)}\exp\left(-\frac{2(r-\Delta d\cdot i)^2}{w_0^2\left(1+\left(\frac{z}{z_R}\right)^2\right)}\right) \tag{8}$$

式中，n表示横向扫描的路径数量。

2　实验结果

2.1　激光烧蚀4H-SiC的表面形貌

为了研究飞秒激光重复扫描加工4H-SiC的表面形貌，需要先分析飞秒激光单线扫描加工4H-SiC的表

面形貌。实验中设置飞秒激光的单脉冲能量为 10 μJ。首先将 4H-SiC 样品固定在飞秒激光加工系统的 XYZ 3 轴运动平台上，使样品的$[11\bar{2}0]$晶向与 X 轴平行，飞秒激光依次从 $-X$ 向 $+X$、从 $+Y$ 向 $-Y$ 扫描样品，加工后样品表面形貌如图 5(a)所示。然后将样品旋转 90°，使样品的$[11\bar{2}0]$晶向与 X 轴垂直，飞秒激光扫描方向同上，加工后样品表面形貌如图 5(b)所示。从图中可以看出，样品表面产生了平行于 X 轴方向的激光诱导周期性条纹和垂直于 X 轴方向的激光诱导微沟槽，微沟槽宽度在 800 nm 左右。激光诱导周期性条纹和激光诱导微沟槽的方向与晶向无关，分别垂直和平行于激光的偏振方向。

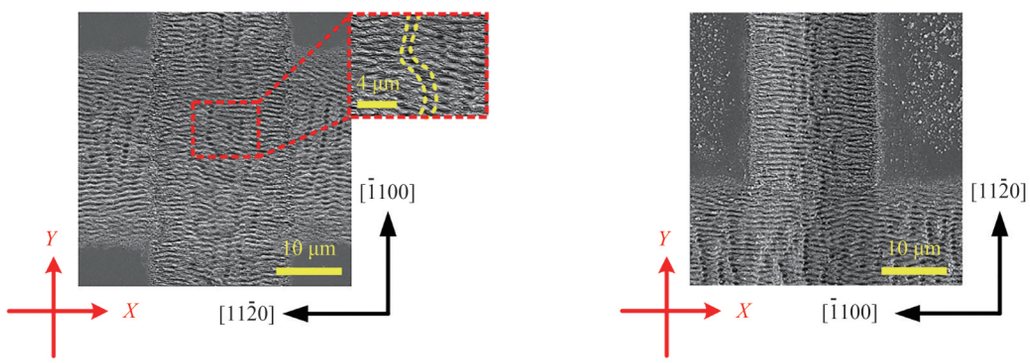

(a) The [11$\bar{2}$0] crystal orientation of 4H-SiC is parallel to the *X*-axis

(b) The [11$\bar{2}$0] crystal orientation of 4H-SiC is perpendicular to the *X*-axis

图 5 飞秒激光单线扫描加工 4H-SiC 后的 SEM 图

Fig.5 SEM images of 4H-SiC processed by femtosecond laser for single-line scanning

2.2 深度方向步进间距对烧蚀深度和表面形貌的影响

实验中设置飞秒激光的单脉冲能量为 30 μJ，扫描线间距 $\Delta d=20$ μm，采用图 2(b)所示的路径 1 加工 4H-SiC，其中 $\theta=90°$。图 6(a)为飞秒激光加工 1 圈后 4H-SiC 样品(标记为“样品 1”)的 SEM 图，采用轮廓仪测得单圈烧蚀深度为 2.9 μm。然后分别设置 $\Delta H=2.9$ μm 和 $\Delta H=15$ μm，以图 2(d)所示的圆柱形材料去除方式加工 4H-SiC 衬底 26 圈(分别标记为“样品 2”和“样品 3”)，预期烧蚀深度为 2.9 μm × 26 = 75.4 μm，加工完成后样品表面形貌和烧蚀深度分别如图 6(b)和(c)所示。样品 2 的烧蚀深度比预期烧蚀深度大 15.6%，且样品 2 被加工表面出现了孔洞，密度为 434 个/mm^2，直径约为 13 μm。样品 3 的烧蚀深度比预期烧蚀深度小 10.2%，被加工表面并未出现孔洞。

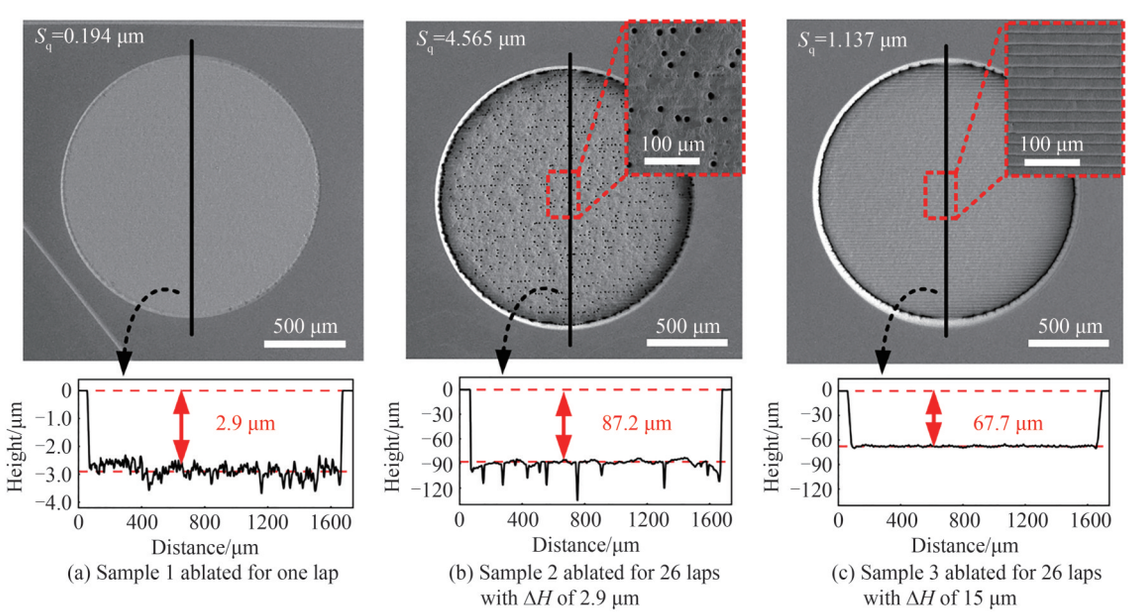

(a) Sample 1 ablated for one lap

(b) Sample 2 ablated for 26 laps with ΔH of 2.9 μm

(c) Sample 3 ablated for 26 laps with ΔH of 15 μm

图 6 不同加工圈数和不同 ΔH 的 4H-SiC SEM 图

Fig.6 SEM images of 4H-SiC with different number of processing laps or ΔH

由于样品3的ΔH=15 μm＞2.9 μm，随着加工平台的上移，样品3被加工表面逐渐远离飞秒激光的束腰位置。被烧蚀表面的激光光强从图4(a)中z=0(束腰位置)所示的光强分布逐渐向$z=z_R$(瑞利长度位置)所示的光强分布过渡，激光能量逐渐分散，并且激光光强在瑞利长度范围内可近似看作线性变化。当加工到26圈时，样品被加工表面距离束腰位置(15－2.9)×26＝314.6 μm＜z_R＝516.5 μm，此时激光的最大光强＞50% I_0。因此，样品3在加工过程中，被烧蚀表面的最大光强逐渐线性减小，烧蚀深度小于预期烧蚀深度。

当扫描线间距Δd=20 μm时，不同横截面内的叠加光强如图7所示。当ΔH=2.9 μm时，采用束腰位置的光斑加工，两次扫描叠加光强的波峰在各自扫描路径中心，波谷在两次扫描路径中间。波峰和波谷的激光光强相差较大，导致样品2被加工表面的波动较大。此外，样品2上孔洞可能与激光能量的不均匀分布有关。当ΔH=15 μm时，加工光斑的激光光强逐渐从z=0向$z=z_R$过渡，波峰与波谷之间的光强差逐渐减小，且波峰逐渐从两次扫描路径中心向重合区域转移，激光能量逐渐分散，因此样品3被加工表面更加平整。

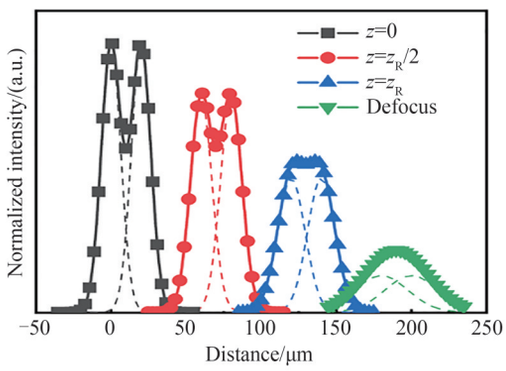

图7　Δd=20 μm时不同横截面的叠加光强

Fig.7　Schematic illustration of the superposition of light intensity in different cross-sections with the Δd of 20 μm

进一步，采用相同的激光参数，通过控制加工圈数来探究样品2中孔洞产生的原因，加工结果如图8所示。由于微沟槽高密度地随机产生在激光扫描路径上，随着加工圈数的增加，微沟槽产生随机重叠，样品表面的微沟槽逐渐变得明显，并在第10圈时，转变为尺寸约为5 μm的凹坑。由于凹坑尺寸远大于微沟槽尺寸，随着加工圈数的进一步增加，微沟槽与凹坑重叠的概率远大于与其他微沟槽重叠的概率，导致凹坑尺寸进一步增大，从而形成孔洞。随着孔洞尺寸的增大，样品表面凹坑数量的增长逐渐变缓。因此，在加工4H-SiC时应尽量使加工样品表面的激光能量分布均匀，并减小微沟槽的重叠概率。

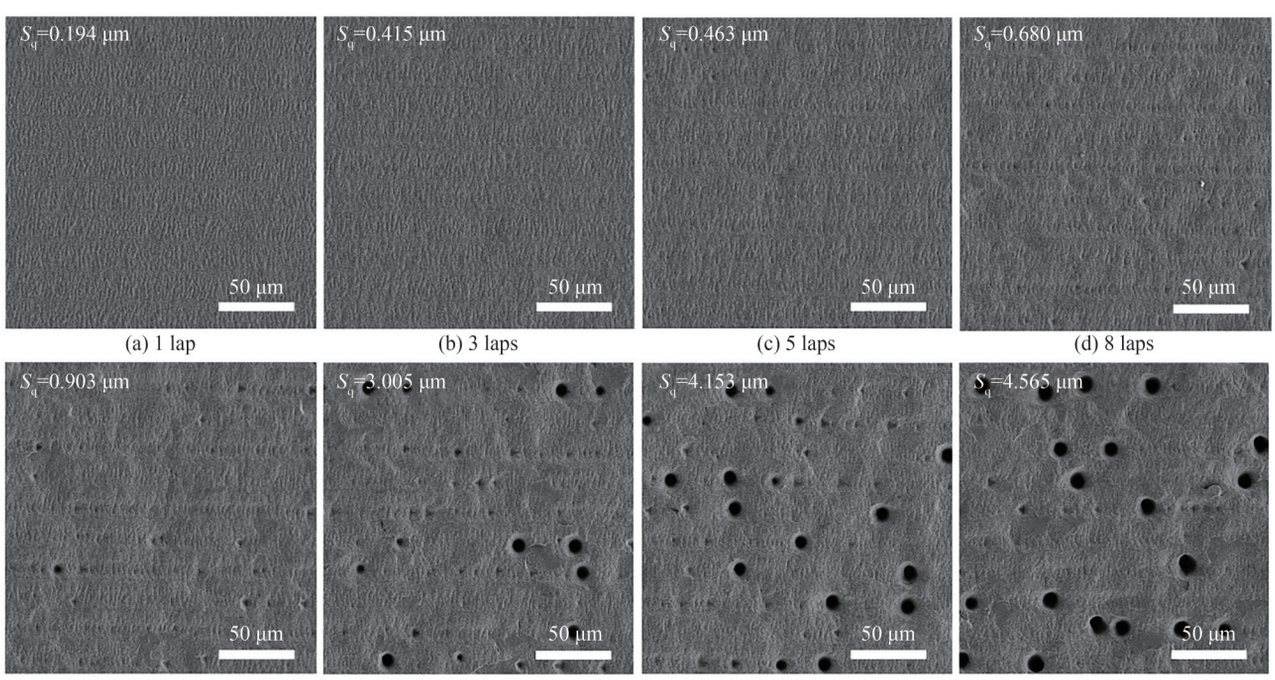

图8　不同加工圈数的4H-SiC被加工表面SEM图

Fig.8　SEM images for the ablated surface of 4H-SiC with different number of processing laps

2.3 扫描路径方向对表面形貌的影响

实验中设置飞秒激光的单脉冲能量为30 μJ,扫描线间距△d=20 μm,深度方向步进间距△H=2.9 μm,采用图2(b)和(c)所示的路径1和路径2扫描,其中θ=90°,60°,30°,0°,以图2(d)所示的圆柱形材料去除方式加工4H-SiC衬底10圈,加工结果如图9所示。随着θ的减小,样品表面粗糙度逐渐增大,表面孔洞的数量逐渐增加。因为随着θ的减小,微沟槽与扫描路径之间的夹角逐渐减小,增大了扫描路径上微沟槽重叠的概率,导致样品表面产生孔洞。对于采用同心圆扫描路径的样品,激光光斑相对于圆心从X轴向Y轴运动时,其路径与偏振方向夹角θ逐渐从0°变为90°,微沟槽重叠的概率逐渐减小。因此采用同心圆扫描方式加工的样品表面的孔洞主要集中在圆心左右两侧45°的扇形区域内,圆心上下两侧45°的扇形区域内基本没有孔洞,且圆心左右两侧的表面RMS粗糙度值与θ=0°样品的表面RMS粗糙度值接近,圆心上下两侧的表面RMS粗糙度值与θ=90°的样品表面RMS粗糙度值接近。因此,在采用飞秒激光加工4H-SiC时,应使飞秒激光的扫描方向垂直于激光偏振方向,即保证微沟槽方向与扫描方向垂直,减小微沟槽之间重叠的概率,进一步减小孔洞形成的概率。

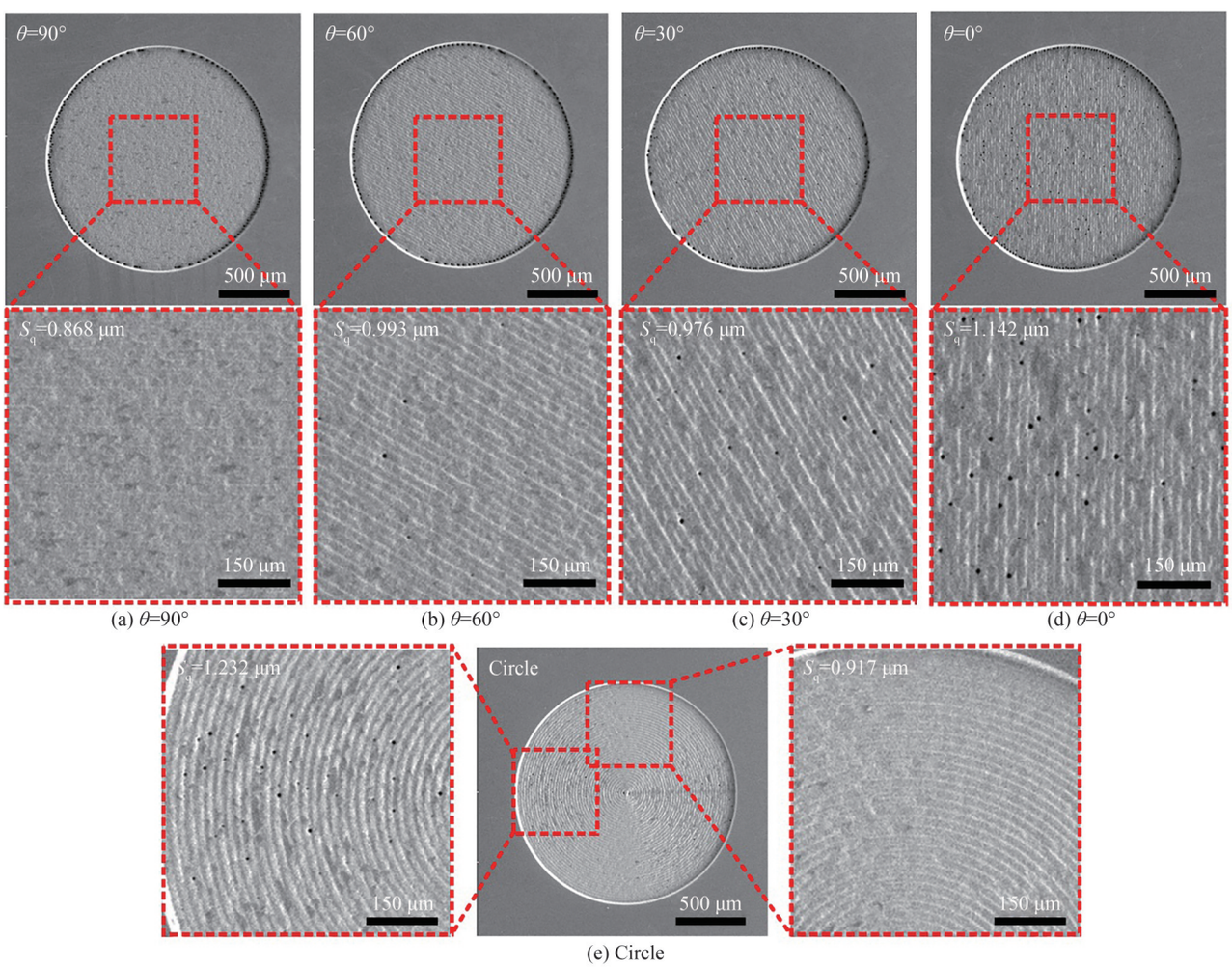

图9 采用不同扫描方向加工4H-SiC后的SEM图

Fig.9 SEM images of 4H-SiC samples processed with different scanning directions

2.4 单脉冲能量对烧蚀深度和RMS粗糙度的影响

实验中设置飞秒激光的单脉冲能量为5,10,15,20,25,30 μJ,扫描线间距为20,15,10,8,5,4,3,2 μm,采用图2(b)所示的路径1加工4H-SiC一圈,其中θ=90°,加工完成后4H-SiC的单圈烧蚀深度和表面RMS粗糙度如图10(a)和(c)所示。如图10(b)所示,在同一横截面内,激光光强随激光单脉冲能量的增加线性增大,因此烧蚀深度随着单脉冲能量的增加逐渐增大。图10(d)显示了在同一横截面内不同单脉冲能量下的叠加光强分布,随着激光单脉冲能量的增加,叠加光强的波峰与波谷之间的光强差也逐渐增大,光强分布更

加不均匀，因此表面RMS粗糙度随着单脉冲能量的增加逐渐增大。

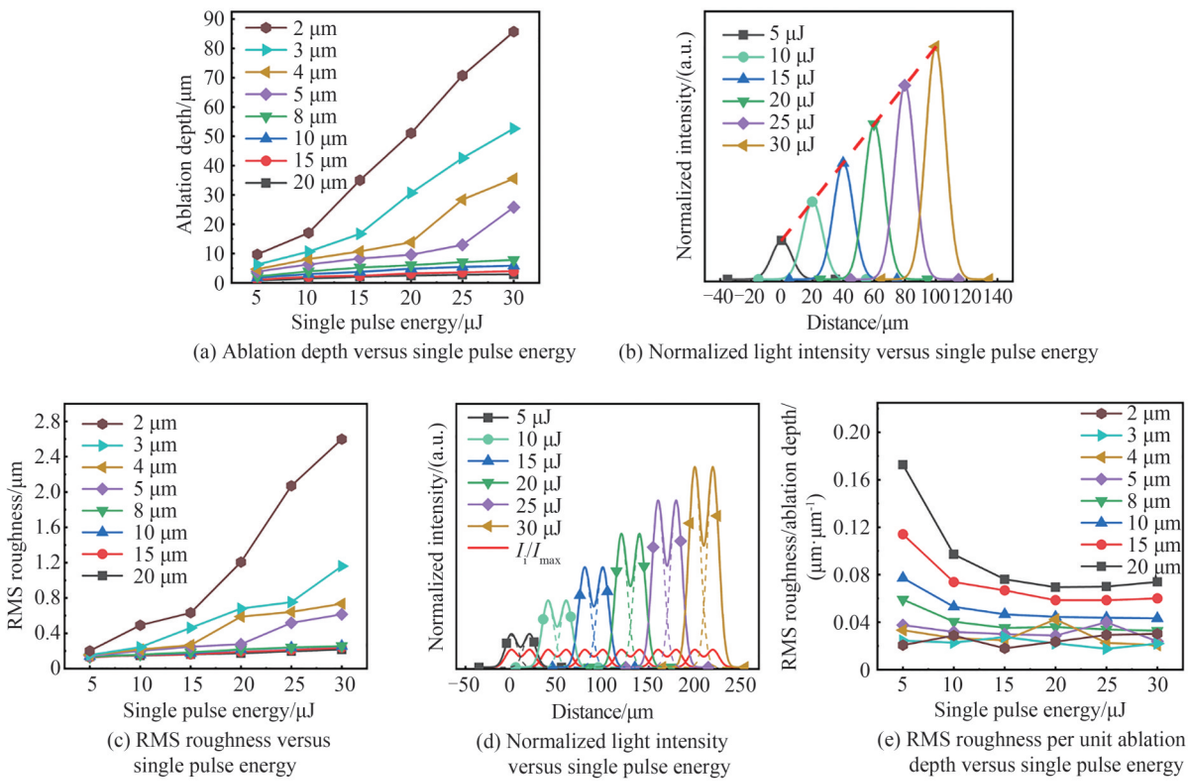

图10　飞秒激光单圈烧蚀深度、光强、烧蚀表面RMS粗糙度、叠加光强、单位烧蚀深度的RMS粗糙度与激光单脉能量的关系

Fig.10　The dependence of the ablation depth for one lap, light intensity, RMS roughness of the ablated surface, the superposition of light intensity, and RMS roughness per unit ablation depth on laser single pulse energy

进一步分析了飞秒激光的单脉冲能量对单位烧蚀深度的RMS粗糙度（$S_{q/H}$）的影响，如图10(e)所示。图10(d)中的I_i/I_{max}表示不同单脉冲能量下同一横截面内各个位置的光强与最大光强的比值。由于光强与烧蚀深度呈正相关，因此I_i/I_{max}的分布可近似反映单位光强的烧蚀深度和烧蚀形貌。从图中可以看出，不同单脉冲能量下的I_i/I_{max}在同一横截面的分布一致，即不同单脉冲能量下的单位光强烧蚀深度和烧蚀形貌一致。因此扫描间隔为5，4，3，2 μm时，$S_{q/H}$基本保持不变。而当扫描间隔为20，15，10，8 μm且单脉冲能量较小时，单圈烧蚀深度较小，其对应的$S_{q/H}$值受扫描路径上的微沟槽影响而偏大。随着单脉冲能量的增加，单圈烧蚀深度逐渐增大，微沟槽的影响逐渐减小，$S_{q/H}$值逐渐趋于稳定。

2.5　扫描线间距对烧蚀深度和RMS粗糙度的影响

在2.4节的基础上，将变量改为扫描线间距$\triangle d$，其结果如图11(a)和(c)所示。如图11(b)所示，在同一横截面内，飞秒激光的叠加光强随扫描线间距的增大呈指数下降，因此烧蚀深度随扫描线间距的增大呈指数下降。RMS粗糙度的变化趋势与烧蚀深度变化趋势相同，这与2.4节的规律一致。进一步分析了扫描线间距$\triangle d$对$S_{q/H}$值的影响。图11(e)显示了同一横截面内不同扫描线间距下叠加光强的I_i/I_{max}的分布图，随着$\triangle d$的增加，I_i/I_{max}的波动逐渐增大，即单位烧蚀深度的样品表面波动逐渐增大，因此$S_{q/H}$值随着扫描线间距的增加逐渐增大。图11(f)～(i)分别显示了扫描线间距$\triangle d$=20，10，5，2 μm时样片被加工表面形貌，随着扫描线间距的减小，被加工表面的微沟槽逐渐减少，说明缩小扫描线间距能够平滑样品被加工表面，减小表面产生孔洞缺陷的概率。因此在飞秒激光加工4H-SiC时，应采用较小的扫描线间距。

设置飞秒激光扫描线间距为2 μm，采用平行线扫描加工4H-SiC，扫描路径方向与激光偏振方向夹角θ=90°，通过控制飞秒激光单脉冲能量和加工圈数即可加工出任意深度的盲孔。本文所需敏感膜片厚度为100 μm，即盲孔深度为250 μm。当飞秒激光单脉冲能量为30 μJ时，单圈烧蚀深度为85.3 μm，则只需加工3圈即可达到预期深度，预期误差为+2.4%。进一步，采用上述参数分别以图2(d)和(e)所示的方式加工4H-SiC，加工结果如图12所示。从图中可以看出，4H-SiC的加工深度分别为244.2 μm和245.4 μm，实际加

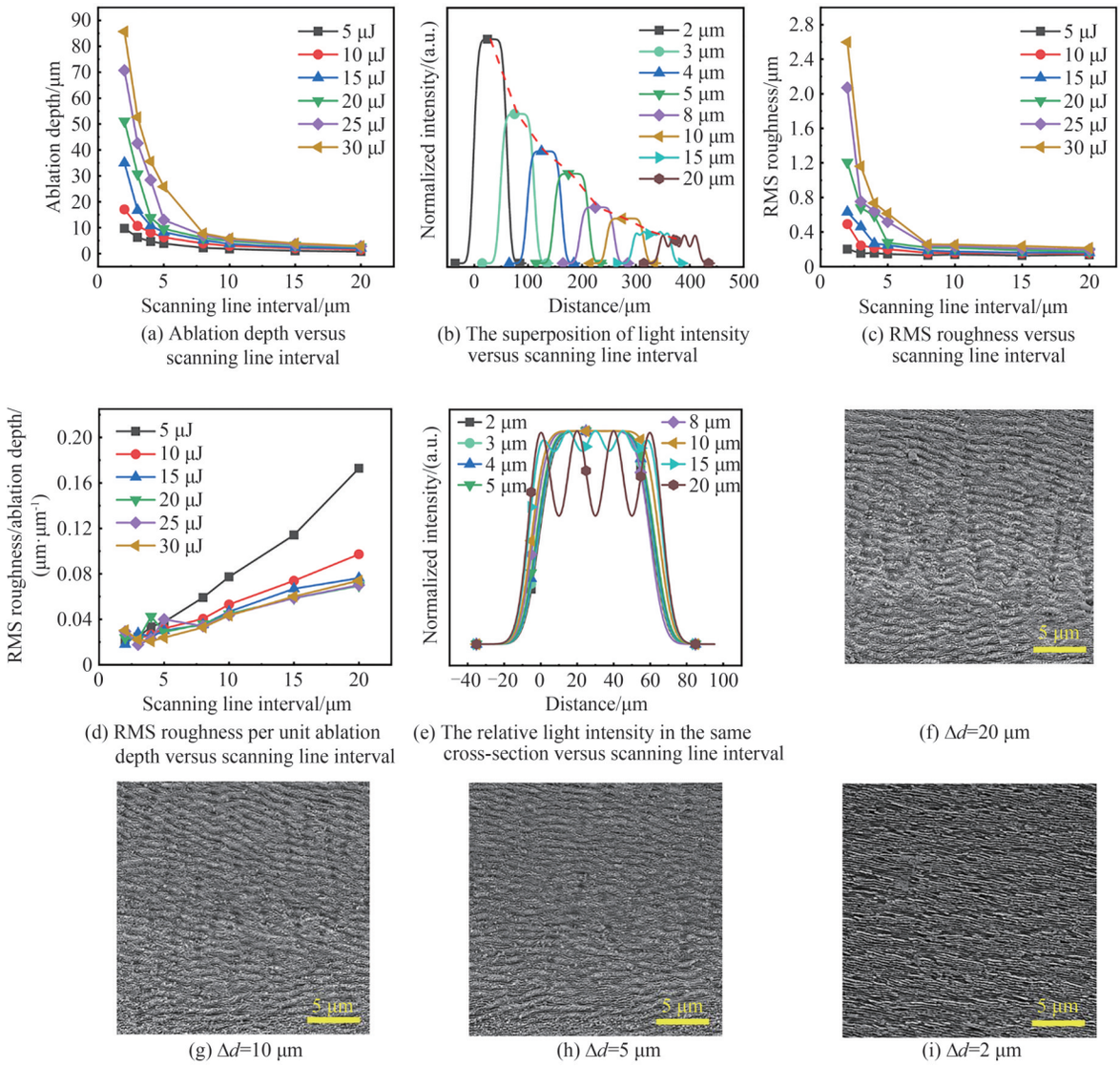

图 11 飞秒激光单圈烧蚀深度、叠加光强、烧蚀表面 RMS 粗糙度、单位烧蚀深度的 RMS 粗糙度、相对光强、表面形貌与扫描线间距的关系

Fig.11 The dependence of the ablation depth for one lap, light intensity, RMS roughness of the ablated surface, the superposition of light intensity, and surface morphology on scanning line interval

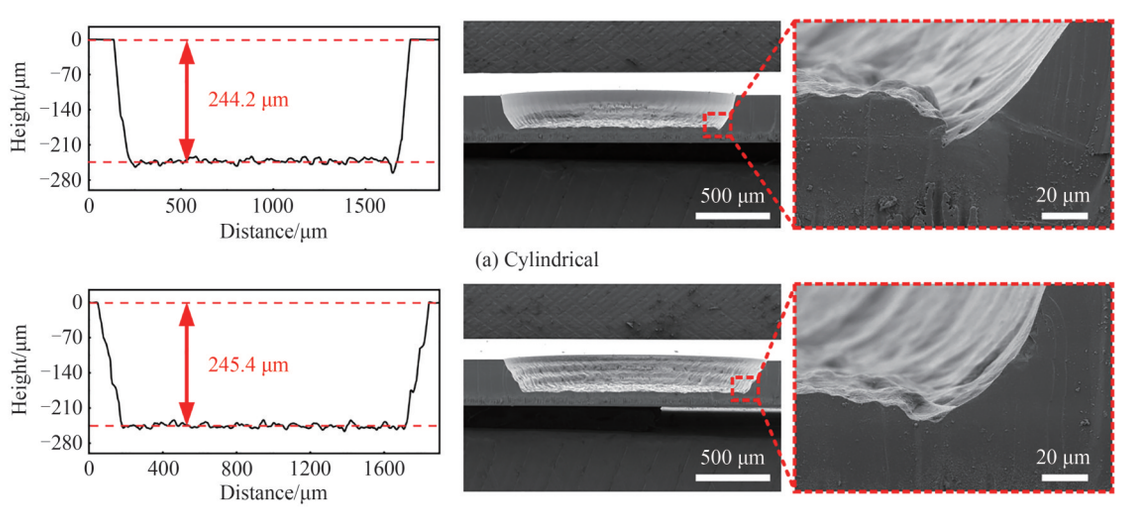

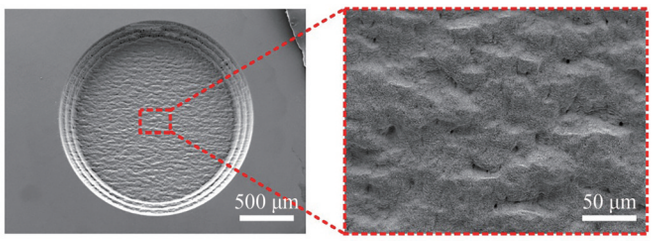

(c) Top-view SEM images of the 4H-SiC pressure sensitive diaphragm

图12　不同材料去除方式加工4H-SiC后的SEM图

Fig.12　SEM images of 4H-SiC samples processed with different material removal methods

工误差为－2.32%和－1.84%，4H-SiC压力敏感膜片表面无明显孔洞，且采用圆台形的材料去除方式能够有效减小4H-SiC敏感膜片与侧壁之间的过烧蚀沟槽深度。

3　结论

本文采用1 028 nm、190 fs飞秒激光系统加工4H-SiC敏感膜片，通过光学轮廓仪和扫描电子显微镜对敏感膜片的烧蚀深度、RMS粗糙度和表面形貌进行了表征。研究了深度方向步进间距、扫描路径方向、单脉冲能量、扫描线间距对4H-SiC烧蚀速率和表面形貌的影响，实验结果表明，4H-SiC样品表面孔洞的形成主要与激光诱导微沟槽的重叠有关。通过使激光加工光斑远离束腰位置或缩小扫描线间距能够使激光能量分布更均匀，有效减少了4H-SiC被烧蚀表面的激光诱导微沟槽的数量；通过增大激光扫描路径与激光偏振方向的夹角有效降低了激光诱导微沟槽的重叠概率，抑制了4H-SiC样品被烧蚀表面上孔洞的形成。最终设置飞秒激光单脉冲能量为30 μJ、扫描路径与激光偏振方向夹角为90°、扫描线间距为2 μm，采用圆台形材料去除方式加工直径为1 600 μm、深度为250 μm的4H-SiC盲孔，单圈烧蚀深度为85.7 μm，加工三圈后得到厚度为100 μm的4H-SiC敏感膜片。所得4H-SiC压力敏感膜片表面无明显孔洞，边缘过烧蚀深度小于10 μm，实现了4H-SiC压力敏感膜片的低损伤飞秒激光加工。

参考文献

[1] AYYILDIZ E, CETIN H, HORVÁTH Z J. Temperature dependent electrical characteristics of Sn/p-Si Schottky diodes [J]. Applied Surface Science, 2005, 252(4): 1153-1158.

[2] ÇALDIRAN Z, DENIZ A R, MEHMET COŞKUN F, et al. I-V-T (current-voltage-temperature) characteristics of the Au/Anthraquinone/p-Si/Al junction device[J]. Journal of Alloys and Compounds, 2014, 584: 652-657.

[3] WU Chen, FANG Xudong, LIU Feng, et al. High speed and low roughness micromachining of silicon carbide by plasma etching aided femtosecond laser processing[J]. Ceramics International, 2020, 46(11): 17896-17902.

[4] AZEVEDO R G, JONES D G, JOG A V, et al. A SiC MEMS resonant strain sensor for harsh environment applications[J]. IEEE Sensors Journal, 2007, 7(4): 568-576.

[5] NAKAO S, ANDO T, SHIKIDA M, et al. Mechanical properties of a micron-sized SCS film in a high-temperature environment[J]. Journal of Micromechanics and Microengineering, 2006, 16(4): 715-720.

[6] RABIER J, RENAULT P O, EYIDI D, et al. Plastic deformation of silicon between 20 ℃ and 425 ℃[J]. Physica Status Solidi C, 2007, 4(8): 3110-3114.

[7] REN J, WARD M, KINNELL P, et al. Plastic deformation of micromachined silicon diaphragms with a sealed cavity at high temperatures[J]. Sensors, 2016, 16(2): 204.

[8] NGUYEN T, PHAN H, DINH T, et al. Highly sensitive 4H-SiC pressure sensor at cryogenic and elevated temperatures[J]. Materials & Design, 2018, 156: 441-445.

[9] SHI Yunbo, SUN Yanan, LIU Jun, et al. UV nanosecond laser machining and characterization for SiC MEMS sensor application[J]. Sensors and Actuators A: Physical, 2018, 276: 196-204.

[10] MIDDELBURG L M, van ZEIJL H W, VOLLEBREGT S, et al. Toward a self-sensing piezoresistive pressure sensor for all-SiC monolithic integration[J]. IEEE Sensors Journal, 2020, 20(19): 11265-11274.

[11] GAO Bo, ZHAI Wenjie, ZHAI Quan, et al. Electro-chemical mechanical polishing of 4H-SiC for scratch-free surfaces with less oxide layer at high efficiency[J]. ECS Journal of Solid State Science and Technology, 2019, 8(11): 677-684.

[12] CHEN Gaopan, LI Jiangguo, LUO Haimei, et al. One-step fabrication of fine surfaces via femtosecond laser on sliced SiC[J]. Materials Science in Semiconductor Processing, 2021, 132: 105926.

[13] OSIPOV A A, IANKEVICH G A, SPESHILOVA A B, et al. High-temperature etching of SiC in SF_6/O_2 inductively

coupled plasma[J]. Scientific Reports, 2020, 10(1): 19977.
[14] ZHUANG Dejin, EDGAR J H. Wet etching of GaN, AlN, and SiC: a review[J]. Materials Science and Engineering: R: Reports, 2005, 48(1): 1-46.
[15] LIU Xinfang, YAN Guoguo, SANG Ling, et al. Defect appearance on 4H-SiC homoepitaxial layers via molten KOH etching[J]. Journal of Crystal Growth, 2020, 531: 125359.
[16] ZHANG Yi, CHEN Hongyingnan, LIU Dianzi, et al. High efficient polishing of sliced 4H-SiC (0001) by molten KOH etching[J]. Applied Surface Science, 2020, 525: 146532.
[17] LUNA L E, TADJER M J, ANDERSON T J, et al. Deep reactive ion etching of 4H-SiC via cyclic SF_6/O_2 segments[J]. Journal of Micromechanics and Microengineering, 2017, 27(9): 95004.
[18] SUNG Hokun, QIANG Tian, YAO Zhao, et al. Vertical and bevel-structured SiC etching techniques incorporating different gas mixture plasmas for various microelectronic applications[J]. Scientific Reports, 2017, 7: 3915.
[19] DOWLING K M, RANSOM E H, SENESKY D G. Profile evolution of high aspect ratio silicon carbide trenches by inductive coupled plasma etching[J]. Journal of Microelectromechanical Systems, 2017, 26(1): 135-142.
[20] HUFF M, PEDERSEN M. Electrical field-induced faceting of etched features using plasma etching of fused silica[J]. Journal of Applied Physics, 2017, 122(2): 23302.
[21] LI Weinan, ZHANG Ruoheng, LIU Yongsheng, et al. Effect of different parameters on machining of SiC/SiC composites via pico-second laser[J]. Applied Surface Science, 2016, 364: 378-387.
[22] RETHFELD B, SOKOLOWSKI-TINTEN K, von der LINDE D, et al. Timescales in the response of materials to femtosecond laser excitation[J]. Applied Physics A, 2004, 79(4): 767-769.
[23] WANG Lukang, ZHAO You, YANG Zixuan, et al. Femtosecond laser micromachining in combination with ICP etching for 4H-SiC pressure sensor membranes[J]. Ceramics International, 2021, 47(5): 6397-6408.
[24] XIE Xiaozhu, PENG Qingfa, CHEN Gaopan, et al. Femtosecond laser modification of silicon carbide substrates and its influence on CMP process[J]. Ceramics International, 2021, 47(10): 13322-13330.
[25] TOMITA T, KINOSHITA K, MATSUO S, et al. Distinct fine and coarse ripples on 4H-SiC single crystal induced by femtosecond laser irradiation[J]. Japanese Journal of Applied Physics, 2006, 45(4L): 444-446.
[26] OKADA T, KAWAHARA H, ISHIDA Y, et al. Cross-sectional TEM analysis of laser-induced ripple structures on the 4H-SiC single-crystal surface[J]. Applied Physics A, 2008, 92(3): 665-668.
[27] YAMAGUCHI M, UENO S, KUMAI R, et al. Raman spectroscopic study of femtosecond laser-induced phase transformation associated with ripple formation on single-crystal SiC[J]. Applied Physics A, 2010, 99(1): 23-27.
[28] TOMITA T, OKADA T, KAWAHARA H, et al. Microscopic analysis of carbon phases induced by femtosecond laser irradiation on single-crystal SiC[J]. Applied Physics A, 2010, 100(1): 113-117.
[29] VARLAMOVA O, REIF J, VARLAMOV S, et al. The laser polarization as control parameter in the formation of laser-induced periodic surface structures: Comparison of numerical and experimental results[J]. Applied Surface Science, 2011, 257(12): 5465-5469.
[30] PECHOLT B, VENDAN M, DONG Yuanyuan, et al. Ultrafast laser micromachining of 3C-SiC thin films for MEMS device fabrication[J]. The International Journal of Advanced Manufacturing Technology, 2008, 39(3-4): 239-250.
[31] DONG Yuanyuan, NAIR R, MOLIAN R, et al. Femtosecond-pulsed laser micromachining of a 4H-SiC wafer for MEMS pressure sensor diaphragms and via holes[J]. Journal of Micromechanics and Microengineering, 2008, 18(3): 35022.
[32] ZHAO You, ZHAO Yulong, WANG Lukang. Application of femtosecond laser micromachining in silicon carbide deep etching for fabricating sensitive diaphragm of high temperature pressure sensor[J]. Sensors and Actuators A: Physical, 2020, 309: 112017.
[33] YE Dahua. Analysis of characteristics of Gaussian beam and its application[J]. Laser Technology, 2019, 43(1): 142-146.
叶大华. 高斯光束特性分析及其应用[J]. 激光技术, 2019, 43(1): 142-146.

Low-damage Micromachining for 4H-SiC Pressure Sensitive Diaphragm by Femtosecond Laser

WAN Zehong[1], DENG Hongyang[1], LEI Yu[2], TAO Guoyi[1], HU Hongpo[3], ZHOU Shengjun[1,2]
(1 *The Institute of Technological Sciences, Wuhan University, Wuhan* 430072, *China*)
(2 *School of Power and Mechanical Engineering, Wuhan University, Wuhan* 430072, *China*)
(3 *School of Automotive Engineering, Guangdong Polytechnic of Science and Technology, Zhuhai* 519090, *China*)

Abstract: As a representative material of the third-generation semiconductor, silicon carbide (SiC)

demonstrates excellent physical properties and chemical stability, which is an ideal material for harsh environment operating devices and high power electronics. To fabricate SiC pressure sensitive components, blind holes are processed on the surface of the SiC substrate to obtain sensitive diaphragms. Laser ablation is an efficient way to process SiC materials, and femtosecond laser processing has been widely studied because of its small thermal effect, low damage to materials, fast processing rate, insensitivity to crystal orientation, and ability to form complex structures.

To investigate the characteristics of 4H-SiC material processed by femtosecond laser, the effects of fabrication process parameters such as step spacing in the depth direction, scanning direction, single pulse energy and scan line spacing on the surface morphology and ablation rate of 4H-SiC material are investigated. The 4H-SiC blind hole with a diameter of 1 600 μm, a depth of 250 μm and a thickness of 100 μm is prepared.

To investigate the effect of depth direction step spacing on the ablation depth and surface morphology, the single pulse energy of the femtosecond laser is set to be 30 μJ; the scanning line spacing is set to be 20 μm; the angle between the laser scanning path and the laser polarization direction (θ) is set to be 90°. The parallel line scanning path is used to process 4H-SiC. The step spacing in the depth direction is set as 2.9 μm and 15 μm. These two samples are marked as sample 2 and sample 3, respectively. The ablation depth of sample 2 was 15.6% larger than the expected ablation depth, and holes appeared on the surface. The ablation depth of sample 3 was 10.2% smaller than the expected ablation depth, and no holes appeared.

To investigate the effect of scan path on surface morphology, the single pulse energy is set to be 30 μJ; the scanning line spacing is 20 μm, the step spacing is 2.9 μm; θ is 90°, 60°, 30°, and 0°. The surface roughness of the sample gradually increases with decreasing θ and the number of surface holes gradually increases. This is because the angle between the microgrooves and the scan path gradually decreases with the decreasing θ, leading to an increase inthe probability of overlapping microgrooves on the scan path and thus the generation of holes on the sample surface.

To investigate the effect of single pulse energy on the ablation depth and surface roughness, the single pulse energy is set to be 5, 10, 15, 20, 25, 30 μJ; θ is 90°; the scanning line spacing is 20, 15, 10, 8, 5, 4, 3, 2 μm. The laser light intensity increases linearly with the increase of the laser single pulse energy. As a result, the ablation depth gradually increases with the increase of the single pulse energy. With the increase of laser single pulse energy, the light intensity distribution is more uneven, resulting in a gradual increase in the surface roughness. Furthermore, the superimposed light intensity of the femtosecond laser decreases exponentially with the increase of the scan line spacing by changing the scanning line spacing. As a result, the ablation depth decreases exponentially with the increase of the scan line spacing.

In this paper, a 1 028 nm, 190 fs femtosecond laser system is used to process 4H-SiC sensitive diaphragms. The experimental results show that the formation of holes on the surface of 4H-SiC samples is related to the overlap of laser-induced microgrooves. The final setting of the femtosecond laser with a single pulse energy of 30 μJ, a scan path angle of 90° to the laser polarization direction, and a scan line spacing of 2 μm is used to process blind holes with a diameter of 1 600 μm and a depth of 250 μm using a circular table-shaped material removal method. The ablation depth of a single turn is 85.7 μm, and the 4H-SiC sensitive diaphragm with a thickness of 100 μm is obtained after three turns of processing. The resulting 4H-SiC pressure-sensitive diaphragm has no obvious holes on the surface, the edge over-ablation depth is less than 10 μm, and the low-damage femtosecond laser processing of 4H-SiC pressure-sensitive diaphragm is obtained.

Key words: Micro-nano machining; Pressure sensitive diaphragm; Femtosecond laser ablation; Silicon carbide; Surface morphology

OCIS Codes: 140.7090; 230.4000; 160.6000; 130.6010

Foundation item: National Natural Science Foundation of China (Nos. 52075394, 51675386, 51775387), National Key Research and Development Program of China (No. 2017YFB1104900), National Youth Talent Support Program